Lawrence Berkeley National Laboratory

Title
A study of extraterrestrial antineutrino sources with the KamLAND detector

Permalink
https://escholarship.org/uc/item/828630t8

Author
Gando, A.

Publication Date
2011-11-01

A study of extraterrestrial antineutrino sources with the KamLAND detector

A. Gando, Y. Gando, K. Ichimura, H. Ikeda, K. Inoue[1], Y. Kibe[2], Y. Kishimoto, M. Koga[1],
Y. Minekawa, T. Mitsui, T. Morikawa, N. Nagai, K. Nakajima K. Nakamura[1], K. Narita,
I. Shimizu, Y. Shimizu, J. Shirai, F. Suekane, A. Suzuki, H. Takahashi, N. Takahashi,
Y. Takemoto, K. Tamae, H. Watanabe, B.D. Xu, H. Yabumoto, H. Yoshida, and S. Yoshida

Research Center for Neutrino Science, Tohoku University, Sendai 980-8578, Japan

S. Enomoto[3], A. Kozlov, and H. Murayama[4]

*Institute for the Physics and Mathematics of the Universe, Tokyo University, Kashiwa 277-8568,
Japan*

C. Grant, G. Keefer[5], and A. Piepke[1]

Department of Physics and Astronomy, University of Alabama, Tuscaloosa, Alabama 35487, USA

T.I. Banks, T. Bloxham, J.A. Detwiler, S.J. Freedman[1], B.K. Fujikawa[1], K. Han, R. Kadel,
T. O'Donnell, and H.M. Steiner

*Physics Department, University of California, Berkeley and
Lawrence Berkeley National Laboratory, Berkeley, California 94720, USA*

D.A. Dwyer, R.D. McKeown, and C. Zhang

*W. K. Kellogg Radiation Laboratory, California Institute of Technology, Pasadena, California
91125, USA*

B.E. Berger

Department of Physics, Colorado State University, Fort Collins, Colorado 80523, USA

C.E. Lane, J. Maricic, and T. Miletic[6],

Physics Department, Drexel University, Philadelphia, Pennsylvania 19104, USA

M. Batygov[7], J.G. Learned, S. Matsuno, and M. Sakai

*Department of Physics and Astronomy, University of Hawaii at Manoa, Honolulu, Hawaii 96822,
USA*

G.A. Horton-Smith[1]

Department of Physics, Kansas State University, Manhattan, Kansas 66506, USA

K.E. Downum and G. Gratta

Physics Department, Stanford University, Stanford, California 94305, USA

Y. Efremenko[1], Y. Kamyshkov, and O. Perevozchikov[8],

Department of Physics and Astronomy, University of Tennessee, Knoxville, Tennessee 37996,
USA

H.J. Karwowski, D.M. Markoff, and W. Tornow

Triangle Universities Nuclear Laboratory, Durham, North Carolina 27708, USA and
Physics Departments at Duke University, North Carolina Central University, and the University
of North Carolina at Chapel Hill

K.M. Heeger[1]

Department of Physics, University of Wisconsin, Madison, Wisconsin 53706, USA

and

M.P. Decowski[1]

Nikhef, Science Park, Amsterdam, the Netherlands

ABSTRACT

We present the results of a search for extraterrestrial electron antineutrinos ($\overline{\nu}_e$'s)
in the energy range $8.3\,\mathrm{MeV} < E_{\overline{\nu}_e} < 30.8\,\mathrm{MeV}$ using the KamLAND detector. In an
exposure of 4.53 kton-year, we identify 25 candidate events. All of the candidate events

---

[1]Also with the Institute for the Physics and Mathematics of the Universe, Tokyo University, Kashiwa 277-8568, Japan

[2]Present address: Department of Physics, Tokyo Institute of Technology, Tokyo 152-8551, Japan

[3]Also with the Center for Experimental Nuclear Physics and Astrophysics, University of Washington, Seattle, Washington 98195, USA

[4]Also with the Physics Department, University of California, Berkeley and Lawrence Berkeley National Laboratory, Berkeley, California 94720, USA

[5]Present address: Lawrence Livermore National Laboratory, Livermore, California 94550, USA

[6]Present address: Department of Physics and Astronomy, Rowan University, 201 Mullica Hill Road, Glassboro, New Jersey 08028, USA

[7]Present address: SNOLAB, Lively, ON P3Y 1M3, Canada

[8]Present address: Louisiana State University Department of Physics & Astronomy Nicholson Hall, Tower Dr. Baton Rouge, LA 70803-4001, USA

can be attributed to background, most importantly neutral current atmospheric neutrino interactions, setting an upper limit on the probability of ^{8}B solar ν_e's converting into $\overline{\nu}_e$'s at 5.3×10^{-5} (90% C.L.). The present data also allows us to set more stringent limits on the diffuse supernova neutrino flux and on the annihilation rates for light dark matter particles.

Subject headings: neutrinos, diffuse flux, solar antineutrinos, light dark matter

1. Introduction

Ambient electron antineutrinos ($\overline{\nu}_e$'s) of terrestrial origin include geoneutrinos (Araki et al. 2005; Bellini et al. 2010), which have energies below $\sim 3.4\,\mathrm{MeV}$, and man-made reactor antineutrinos (Cowan et al. 1956; Vogel et al. 1981), which have energies below $\sim 8\,\mathrm{MeV}$. Naturally produced $\overline{\nu}_e$'s with higher energies must be of cosmic origin. The region above a few tens of MeV is dominated by neutrinos generated from the decays of muons and pions produced by cosmic-ray interactions in the atmosphere. For antineutrinos in the energy region between 8 MeV and 15 MeV, only diffuse neutrino flux from old supernovae (Totani & Sato 1995) and exotic generation mechanisms, e.g., conversion of solar neutrinos into antineutrinos (Okun et al. 1984) or light dark matter annihilation (Palomares-Ruiz & Pascoli 2008) are thought to be possible.

1.1. Solar Antineutrinos

There is no direct production of $\overline{\nu}_e$'s in the Sun. However, if the neutrino has a non-zero magnetic moment it could be converted into an antineutrino in the strong solar magnetic field.

This mechanism was originally proposed as a solution to the solar neutrino problem (Okun et al. 1984) and was later revisited in (Akhmedov & Pulido 2003). A two-step process takes place, the first step occurs deep inside the solar interior, where a ν_e converts into a $\overline{\nu}_\mu$ via spin flavor precession. The $\overline{\nu}_\mu$ then oscillates into an $\overline{\nu}_e$ while propagating from the Sun to the Earth. The combined probability for the two processes is

$$P(\nu_{eL} \rightarrow \overline{\nu}_{eR}) \simeq 1.8 \times 10^{-10} \sin^2 2\theta_{12} \left[\frac{\mu}{10^{-12}\mu_B} \frac{B_T(0.05R_\odot)}{10\,\mathrm{kG}} \right]^2, \tag{1}$$

where B_T is the transverse solar magnetic field in the region of neutrino production, $R_\odot$ is the solar radius, and μ is the neutrino magnetic moment in Bohr magneton (μ_B). Very little is known about the magnitude of magnetic fields in the solar interior, but values up to $3 \times 10^7\,\mathrm{G}$ are permitted based on SOHO observations (Couvidat et al. 2003). The present best-limit for the probability of neutrino-to-antineutrino conversion, from the Borexino experiment, is less than 1.3×10^{-4} (Bellini et al. 2011).

1.2. Diffuse Supernova Neutrino Flux

A diffuse $\overline{\nu}_e$ background exists from past core-collapse supernovae. Only upper limits for the diffuse supernova neutrino flux (DSNF) have been set by Super-Kamiokande and SNO for energies above $19.3\,\mathrm{MeV}$ (Malek et al. 2003) and $22.9\,\mathrm{MeV}$ (Aharmim et al. 2006), respectively. Because the diffuse $\overline{\nu}_e$ energy is lowered by redshift, the spectral shape is closely connected to the history of star formation. Various supernova and cosmological models predict different shapes, and should be confronted with data.

1.3. Dark Matter Annihilation

Self-annihilation of light (MeV-range) dark matter in the universe could create a mono-energetic neutrino signal in the detector. The Super-Kamiokande data provides the best-limit on the rate of such annihilation for dark matter mass (m_χ) above $15\,\mathrm{MeV}$. Assuming an annihilation model in the Galactic halo (Palomares-Ruiz & Pascoli 2008), the limit can be translated into a velocity-dependent averaged cross section ($\langle \sigma_A v \rangle$) for dark matter particles.

2. The KamLAND Experiment

KamLAND is located $\sim$1 km under the peak of Mt. Ikenoyama (36.42°N, 137.31°E) near Kamioka, Japan. The 2700 meters water equivalent (mwe) of vertical rock overburden reduces the cosmic ray muon flux by almost five orders of magnitude. A schematic diagram of KamLAND is shown in Fig. 1. The primary target volume consists of 1 kton of ultra-pure liquid scintillator (LS)

contained in a 13-m-diameter spherical balloon made of 135-μm-thick transparent nylon-EVOH (ethylene vinyl alcohol copolymer) composite film. The LS consists of 80% dodecane and 20% pseudocumene (1,2,4-trimethylbenzene) by volume, and 1.36 ± 0.03 g/liter of the fluor PPO (2,5-diphenyloxazole). A buffer comprising 57% isoparaffin and 43% dodecane oils by volume, which fills the region between the balloon and the surrounding 18-m-diameter spherical stainless-steel outer vessel, shields the LS from external radiation. The specific gravity of the buffer oil (BO) is adjusted to be 0.04% lower than that of the LS. An array of photomultiplier tubes (PMTs)—1325 specially developed fast PMTs masked to 17-in.-diameter and 554 older 20-in.-diameter PMTs reused from the Kamiokande experiment (Kume et al. 1983)—are mounted on the inner surface of the stainless-steel, providing 34% photocathode coverage. This inner detector (ID) is shielded by a 3.2-kton water-Cherenkov outer detector (OD).

Electron antineutrinos are detected in KamLAND via the inverse beta-decay reaction,

$$\overline{\nu}_e + p \rightarrow e^+ + n. \tag{2}$$

This process has a delayed-coincidence (DC) event-pair signature which offers powerful background suppression. The energy deposited by the positron, which generates the DC pair's prompt event, is approximately related to the incident $\overline{\nu}_e$ energy by $E_{\overline{\nu}_e} \simeq E_{\mathrm{p}} + \overline{E}_n + 0.8\,\mathrm{MeV}$, where E_{p} is the sum of the e^+ kinetic energy and annihilation γ energies, and $\overline{E}_n$ is the average neutron recoil energy which is of $O(100\,\mathrm{keV})$ for $E_{\mathrm{p}} > 7.5\,\mathrm{MeV}$. The delayed event in the DC pair is generated by a 2.2 MeV γ-ray produced when the neutron captures on a proton. The mean neutron capture time is $(207.5 \pm 2.8)\,\mu\mathrm{s}$ (Abe et al. 2010). The detector is periodically calibrated with γ sources deployed from a glove box installed at the top of the chimney region. The radioactive sources are ^{60}Co, ^{68}Ge, ^{203}Hg, ^{65}Zn, ^{241}Am^{9}Be, ^{137}Cs, and ^{210}Po^{13}C, providing energy calibration up to $\sim 8\,\mathrm{MeV}$ along the central axis of the detector. In addition, capture of neutrons on hydrogen and carbon provides energy calibration throughout the entire sensitive volume. The visible energy in the detector is measured from the number of detected photoelectrons and is corrected for event position, detector non-uniformity, and scintillator non-linearity from quenching and Cherenkov light production. The overall vertex reconstruction resolution is $\sim 12\,\mathrm{cm}\,/\sqrt{E(\mathrm{MeV})}$, and energy resolution is $6.4\%/\sqrt{E(\mathrm{MeV})}$. Energy reconstruction of positrons with $E_{\mathrm{p}} > 7.5\,\mathrm{MeV}$ (i.e., $E_{\overline{\nu}_e} > 8.3\,\mathrm{MeV}$) is verified using tagged ^{12}B β^--decays ($\tau = 29.1\,\mathrm{ms}$, $Q = 13.4\,\mathrm{MeV}$) generated via muon spallation (Abe et al. 2010).

3. Event Selection

The present analysis includes data accumulated between March 5, 2002 and July 23, 2010, corresponding to 2343 live-days. For the present search the following criteria were used: the prompt energy is required to be $7.5\,\mathrm{MeV} < E_{\mathrm{p}} < 30.0\,\mathrm{MeV}$, and the delayed energy to be $1.8\,\mathrm{MeV} < E_{\mathrm{d}} < 2.6\,\mathrm{MeV}$; a fiducial volume cut of $R < 6\,\mathrm{m}$ on both prompt and delayed events, a time correlation cut of $0.5\,\mu\mathrm{s} < \Delta T < 1000\,\mu\mathrm{s}$, and a spatial correlation cut of $\Delta R < 1.6\,\mathrm{m}$, this cut is driven by the mean

free path of capture-γ in the LS rather than the diffusion distance of the neutron. Spallation cuts were used to reduce backgrounds from long-lived isotopes, such as ^{9}Li ($\tau = 257$ ms, $Q = 13.6$ MeV), that are generated by cosmic muons passing through the scintillator: a 2 ms veto is applied to the entire detector volume after a non-showering muon for both prompt and delayed events, a 2 s veto is applied after a showering muon (i.e., muons depositing more than 3 GeV of energy above their minimum ionizing contribution) or non-reconstructed muon, while a 2-s 3-m-radius cylindrical cut is applied around well-reconstructed non-showering muons (Abe et al. 2010) for delayed events. The overall selection efficiency of the candidates is 92%, which is evaluated from a Monte Carlo (MC) simulation.

4. Background Calculations

4.1. Random Coincidences

Two uncorrelated events in the detector may accidentally coincide in time, space, and energy so as to pass the $\overline{\nu}_e$ selection cuts. To estimate the background contribution from random coincidences, events were selected with the appropriate prompt and delayed energies but in an out-of-time interval of 0.2 s to 1.2 s after the prompt event. This out-of-time window is 10^3 times longer than the time interval used for the $\overline{\nu}_e$ selection, providing a high-statistics background measurement. The time distribution between prompt and delayed events in the range between 0.2 s and 1.2 s shows no correlation between these events. The random coincidence background for the analysis is determined to be 0.22 ± 0.01 DC-pairs.

4.2. Reactor Antineutrinos

The location of the KamLAND detector was selected for the copious $\overline{\nu}_e$ flux from 56 Japanese nuclear power plants in order to study neutrino oscillation (Gando et al. 2011). The reactor $\overline{\nu}_e$ flux at KamLAND dominates all other $\overline{\nu}_e$ sources for $E_{\rm p} < 7.5$ MeV. However, the tail of the reactor neutrino energy distribution extends to higher energies. The $\overline{\nu}_e$ flux comes primarily from the beta-decay of neutron-rich fragments produced in the fission of four isotopes: ^{235}U, ^{238}U, ^{239}Pu, and ^{241}Pu. For each reactor the appropriate operational records including thermal power generation, fuel burn-up, shutdowns and fuel reload schedule were used to calculate the fission rates. The resulting $\overline{\nu}_e$ spectrum was calculated using the model of (Schreckenbach et al. 1985; Hahn et al. 1989; Vogel et al. 1981). The same methodology was used for previous reactor $\overline{\nu}_e$ analyses and showed excellent agreement over a wide energy range between expected and detected $\overline{\nu}_e$ events when taking neutrino oscillations into account (Gando et al. 2011). The total number of reactor $\overline{\nu}_e$ candidates having $E_{\rm p} > 7.5$ MeV is calculated to be 2.2 ± 0.7 events.

4.3. Radioactive Isotopes

Cosmic-ray muons interacting with carbon nuclei in the scintillator produce a variety of radioactive isotopes (Abe et al. 2010). Two of these isotopes, ^{8}He and ^{9}Li, have decay modes with electrons and neutrons in the final state. Such decays create DC-pairs similar to inverse beta-decay and therefore represent a background in the present study.

The combination of a 2-s veto of the detector after showering muons and a 2-s 3-m-radius cylindrical cut after non-showering muons significantly reduces the contribution of this background, but cannot eliminate it completely. The ^{9}Li isotope, which has a higher end-point value, longer life time and a higher production rate, generates the majority of these background events after cuts. To determine the contribution from this background we selected ^{9}Li candidates using the same cuts that were used for the selection of the $\overline{\nu}_e$ candidates, but the muon veto was not applied. The ^{9}Li rate was evaluated from the distribution of the decay time relative to all previous muons, using a wider energy window of $0.9\,\mathrm{MeV} < E_\mathrm{p} < 15.0\,\mathrm{MeV}$ to reduce statistical errors. For a 6-m fiducial volume, 2074 ± 49 events were found after showering muons and 454 ± 31 events in a 3-m-radius cylinder around the muon track after non-showering muons. 20% of these events occur in the energy region of interest $7.5\,\mathrm{MeV} < E_\mathrm{p} < 15.0\,\mathrm{MeV}$. The 2-s cut reduces the ^{9}Li background from showering muons to less than 0.2 events for $E_\mathrm{p} > 7.5\,\mathrm{MeV}$. As non-showering muons occur with a relatively high frequency (0.2 Hz), to avoid the drastic loss of exposure which would accompany a 2-s full-detector veto we take advantage of the fact that non-showering muons can be relatively well tracked in the LS and instead restrict the 2-s veto to a 3-m-radius cylinder around the muon track. A 2-ms full volume veto after all tagged muons is also used to suppress any spallation neutrons. To measure the efficiency of these cuts the distribution of neutron captures as a function of distance from the muon track was examined, and we found only 5.9% of neutrons survive the 3-m-radius cylindrical cut. The resulting number of ^{9}Li from spallation background with $E_\mathrm{p} > 7.5\,\mathrm{MeV}$ and surviving the 3-m-radius cylindrical cut and time cut is 4.0 ± 0.3 events.

4.4. Fast Neutrons

Fast neutrons outside the inner detector may cause backgrounds in the fiducial volume. A fast neutron can scatter on protons or carbon nuclei in the LS producing a scintillation signal followed by a neutron capture signal, mimicking an $\overline{\nu}_e$ coincidence. A MC simulation of fast neutrons reveals that the dominant background contribution is caused by muon-induced cosmogenic neutrons. A 2-ms veto after OD-tagged muons mostly eliminates this background, while OD-untagged muons and the OD inefficiency cause a residual background. The MC-based study estimates 3.2 ± 3.2 fast neutrons remain in the data set, where a conservative uncertainty of 100% for the simulated neutron production rate by muons is assumed (Abe et al. 2010).

4.5. Atmospheric Neutrino Interactions

Charged current (CC) and neutral current (NC) interactions of atmospheric neutrinos with carbon atoms in the KamLAND scintillator are the most significant source of background. Atmospheric neutrino spectra from (Honda et al. 2007), calculated specifically for the KamLAND location, were used to estimate the contribution from these backgrounds.

The CC reactions by atmospheric $\overline{\nu}_e$'s generate an irreducible background. The contribution from atmospheric $\overline{\nu}_e$'s is estimated to be $\sim$0.06 events in the energy window $7.5\,\mathrm{MeV} < E_\mathrm{p} < 30.0\,\mathrm{MeV}$. Atmospheric ν_μ's and $\overline{\nu}_\mu$'s could react with both protons and carbon nuclei to produce muons and neutrons. The amount of detectable energy is shifted lower for such reactions because a large fraction of the neutrino's initial energy is expended to produce the muon. On the other hand, such reactions are followed by muon decay and therefore manifest themselves as a triple time correlation between the prompt event, muon decay and neutron capture. In the event selection, we found one coincidence event accompanied by a muon decay signal in a decay time interval of 0.5-μs to 10-μs, and excluded it from the candidates. To calculate the contribution from these reactions, the cross sections from (Athar et al. 2007) were employed. The resulting background levels for reactions with a neutron in the final state are listed in Tab. 1. We estimate 4.0 ± 0.9 events in total. The tagging efficiencies of the muon-decay-coincidence signature are calculated to be 78.6% and (77.5 ± 0.2)% from mean life times in carbon of positive and negative muons respectively. The residual background, including an untagged contribution from (7.1 ± 1.4)% of negative muons which capture rather than decay, is 0.9 ± 0.2 events.

The most challenging background to estimate is that from the NC interactions of all neutrino species with carbon. In these reactions the neutrino transfers only a fraction of its energy to the final products. It can eject a neutron from the carbon nucleus, leaving it in an excited state with multiple decay modes. We used the following procedure to calculate the contribution from this background: we integrated the momentum transfer from a neutrino to a quasi-free neutron over the entire atmospheric neutrino spectra (Honda et al. 2007) using cross sections from (Ahrens et al. 1987). We then accounted for the neutron binding energies for P-shell (18.7 MeV) and S-shell (41.7 MeV) configurations and the corresponding shell populations. We also assumed that the neutron was removed from the carbon atom, leaving it in an excited state. All de-excitation modes reported in (Kamyshkov & Kolbe 2003) were taken into account. For each final product we converted the particle energy to visible energy in the detector using an energy scale model that includes non-linearities from scintillator quenching. We calculate the contribution from this background to be 16.4 events with an estimated systematic uncertainty of 29% which is driven by uncertainties in the atmospheric neutrino flux and the cross section of NC neutrino interactions.

We also attempted to estimate the NC background using the NUANCE software tool (version 3), which simulates neutrino interactions and related processes (Casper 2002). However, we found the code overestimates this background rate by a factor of $\sim$2 relative to the above calculation in the energy region under study, mainly due to an inaccurate cross section for intra-nuclear nucleon

re-scattering and an unexpected $\sim 25\,\mathrm{MeV}$ offset of outgoing neutron energies. We therefore do not use the NUANCE-based estimation in this analysis.

5.   Data Interpretation

We observe 25 events after the cuts described in Section 3. The estimated number of backgrounds for $\overline{\nu}_e$ detection summarized in Tab. 2 is 26.9 ± 5.7 events in the prompt energy window $7.5\,\mathrm{MeV} < E_\mathrm{p} < 30.0\,\mathrm{MeV}$. Fig. 2 shows the event distribution as a function of prompt energy. The data set presented here contains 16 times more statistics than the first KamLAND publication on this subject, allowing us to verify the expected background contribution in the analyzed energy window. The data is analyzed using an unbinned maximum likelihood fit to the event spectrum. The estimate for ^{9}Li and reactor $\overline{\nu}_e$ are rather robust, on the other hand, reliable data for neutral current interactions in the energy range of interest do not exist and the method we used to calculate this background contribution has large uncertainties. To avoid possible bias from modeling in the NC background calculation, the normalization of the NC events is a free parameter in the spectral fits.

From the unbinned maximum likelihood fit, the allowed region for the NC background and the probability of solar neutrino conversion is shown in Fig. 3. For the NC-floated normalization analysis, the upper limit for neutrino conversion is 5.3×10^{-5} at 90% C.L., which corresponds to a solar $\overline{\nu}_e$ flux of 93 $\mathrm{cm}^{-2}\mathrm{s}^{-1}$ above the energy threshold ($E_{\overline{\nu}_e} \geq 8.3$ MeV). This limit is a factor 2.5 improvement over the previous limit in (Bellini et al. 2011). The fitted NC background assuming zero solar $\overline{\nu}_e$ events is $14.8^{+5.8}_{-5.4}$ events, which is in good agreement with the calculation (16.4 ± 4.7 events) within the uncertainties.

The probability for solar neutrino conversion can be predicted by the models of spin flavor precession and MSW-LMA oscillations in the Sun. If the conversion model for ^{8}B neutrinos of Eq. (1) is assumed, we obtain the following limit on the product of the neutrino magnetic moment (μ) and the transverse solar magnetic field in the region of neutrino production (B_T):

$$\frac{\mu}{10^{-12}\mu_B}\frac{B_T(0.05R_\odot)}{10\,\mathrm{kG}} < 5.9 \times 10^2, \tag{3}$$

using the value of $34°$ for the mixing angle (Gando et al. 2011). The current best limit on the neutrino magnetic moment is from the GEMMA spectrometer, $\mu_{\overline{\nu}_e} < 3.2 \times 10^{-11}\,\mu_B$ at 90% C.L. (Beda et al. 2010). Lack of knowledge of the value of B_T limits KamLAND sensitivity to the neutrino magnetic moment.

This data also tests other potential $\overline{\nu}_e$ sources. Assuming an energy spectrum from the reference model (Ando & Sato 2004), we found an upper limit for the diffuse supernova $\overline{\nu}_e$ flux of 139 $\mathrm{cm}^{-2}\mathrm{s}^{-1}$ at 90% C.L. in the analyzed energy range. This limit is weaker than our solar $\overline{\nu}_e$ flux limit due to the strong anticorrelation between the signal and NC background events amplified by the similarity in their spectral shapes. This flux limit corresponds to about 36 times the model

prediction (Ando & Sato 2004), indicating poor statistical power in constraining the cosmological models using the current KamLAND data. The upper limit for the monochromatic $\bar{\nu}_e$ flux at each energy can be translated to a limit for the dark matter annihilation cross section (Palomares-Ruiz & Pascoli 2008). The dark matter annihilation limit varies weakly over the dark matter mass range due to limited statistics. We obtain $\langle \sigma_A v \rangle < (1–3) \times 10^{-24}\,\mathrm{cm^3 s^{-1}}$ at 90% C.L. in the mass range 8.3 MeV $< m_\chi <$ 30.8 MeV, as shown in Fig. 4. This is the most stringent constraint on the annihilation cross section below 15 MeV.

Finally, we also present model-independent upper limits for $\bar{\nu}_e$ fluxes, as shown in Fig. 5. The limits are given at 90% C.L. based on the rate analysis using the Feldman-Cousins approach (Feldman & Cousins 1998) with 1 MeV energy bins, including all the constraints on the background estimates in Tab. 2. The KamLAND data provides the best limits in the presented energy range 8.3 MeV $< E_{\bar{\nu}_e} <$ 18.3 MeV, owing to the efficient $\bar{\nu}_e$ detection by the delayed coincidence method and large exposure. Given that data are background limited, mainly from the atmospheric neutrino NC interactions, accumulation of additional statistics is unlikely to improve this limit significantly.

In conclusion, we report the spectrum of high-energy $\bar{\nu}_e$ candidates found in the KamLAND data set accumulated over more than eight years of detector operation. The live time exposure corresponds to 4.53 kton-year. In the energy range from 8.3 MeV to 30.8 MeV, no excess of $\bar{\nu}_e$ events over the expected background consisting of mostly atmospheric neutrino NC interactions, cosmogenically induced radioactivity, and reactor neutrino was detected. The data allow significantly improved limits on solar $\bar{\nu}_e$ conversion probability, and on diffuse supernova neutrino flux and annihilation cross section of dark matter below 15 MeV. The present level of background indicates limitations for future studies of $\bar{\nu}_e$'s in this energy range using KamLAND. While a better detector location could eliminate ^{9}Li background and suppress reactor neutrino background, atmospheric neutrino NC interactions will continue to present significant challenges for next-generation large liquid scintillator detectors.

APPENDIX

The model-independent upper limits for $\overline{\nu}_e$ fluxes provided for each energy may be useful to give an estimate of upper limits for various $\overline{\nu}_e$ sources. For example, one can easily test one's own model with a certain energy spectrum by an appropriate data integration. Tab. 3 lists the 1 MeV binned upper limits shown in Fig. 5. The binned χ^2 is defined as

$$\chi^2 \;\; = \;\; \sum_i \frac{\nu_i^2}{(u_i/\sqrt{2.71})^2} \tag{4}$$

where ν_i is the model expectation for each energy bin, u_i is the KamLAND upper limit at 90% C.L., and $\sqrt{2.71}$ is the conversion factor of limits from 90% C.L. to 1σ C.L. This binned χ^2 analysis approximately reproduces the solar $\overline{\nu}_e$ flux limit which is based on the unbinned maximum likelihood method including all background and systematic uncertainties. On the other hand, a limit for the diffuse supernova $\overline{\nu}_e$ flux based on Eq. (4) will be optimistic, because Tab. 3 data include the constraints on the NC background estimate.

REFERENCES

Abe, S., et al. 2010, Phys. Rev. C, 81, 025807

Aharmim, B., et al. 2004, Phys. Rev. D, 70, 093014

Aharmim, B., et al. 2006, ApJ, 653, 1545

Ahrens, L. A., et al. 1987, Phys. Rev. D, 35, 785

Akhmedov, E. K., & Pulido, J. 2003, Phys. Lett. B, 553, 7

Ando, S., & Sato, K. 2004, New J. Phys., 6

Araki, T., et al. 2005, Nature, 436, 499

Athar, M. S., Ahmad, S., & Singh, S. K. 2007, Phys. Rev. D, 75, 093003

Beda, A. G., Brudanin, V. B., Egorov, V. G., Medvedev, D. V., Pogosov, V. S., Shirchenko, M. V., & Starostin, A. S. 2010, arXiv:1005.2736

Bellini, G., et al. 2010, Phys. Lett. B, 687, 299

Bellini, G., et al. 2011, Phys. Lett. B, 696, 191

Casper, D. 2002, Nucl. Phys. B Proc. Suppl., 112, 161

Couvidat, S., Turck-Chièze, S., & Kosovichev, A. G. 2003, ApJ, 599, 1434

Cowan, C. L., J., Reines, F., Harrison, F. B., Kruse, H. W., & McGuire, A. D. 1956, Science, 124, 103

Feldman, G. J., & Cousins, R. D. 1998, Phys. Rev. D, 57

Gando, A., et al. 2011, Phys. Rev. D, 83

Gando, Y., et al. 2003, Phys. Rev. Lett., 90, 171302

Hahn, A. A., Schreckenbach, K., Gelletly, W., von Feilitzsch, F., Colvin, G., & Krusche, B. 1989, Phys. Lett. B, 218, 365

Honda, M., Kajita, T., Kasahara, K., Midorikawa, S., & Sanuki, T. 2007, Phys. Rev. D, 75, 043006

Kamyshkov, Y., & Kolbe, E. 2003, Phys. Rev. D, 67, 076007

Kume, H., Sawaki, S., Ito, M., Arisaka, K., Kajita, T., Nishimura, A., & Suzuki, A. 1983, Nucl. Instr. Meth. Phys. Res., 205, 443

Malek, M., et al. 2003, Phys. Rev. Lett., 90, 061101

Okun, L. B., et al. 1984, Sov. Phys. JETP, 64, 446

Palomares-Ruiz, S., & Pascoli, S. 2008, Phys. Rev. D, 77, 025025

Schreckenbach, K., Colvin, G., Gelletly, W., & Von Feilitzsch, F. 1985, Phys. Lett. B, 160, 325

Totani, T., & Sato, K. 1995, Astropart. Phys., 3, 367

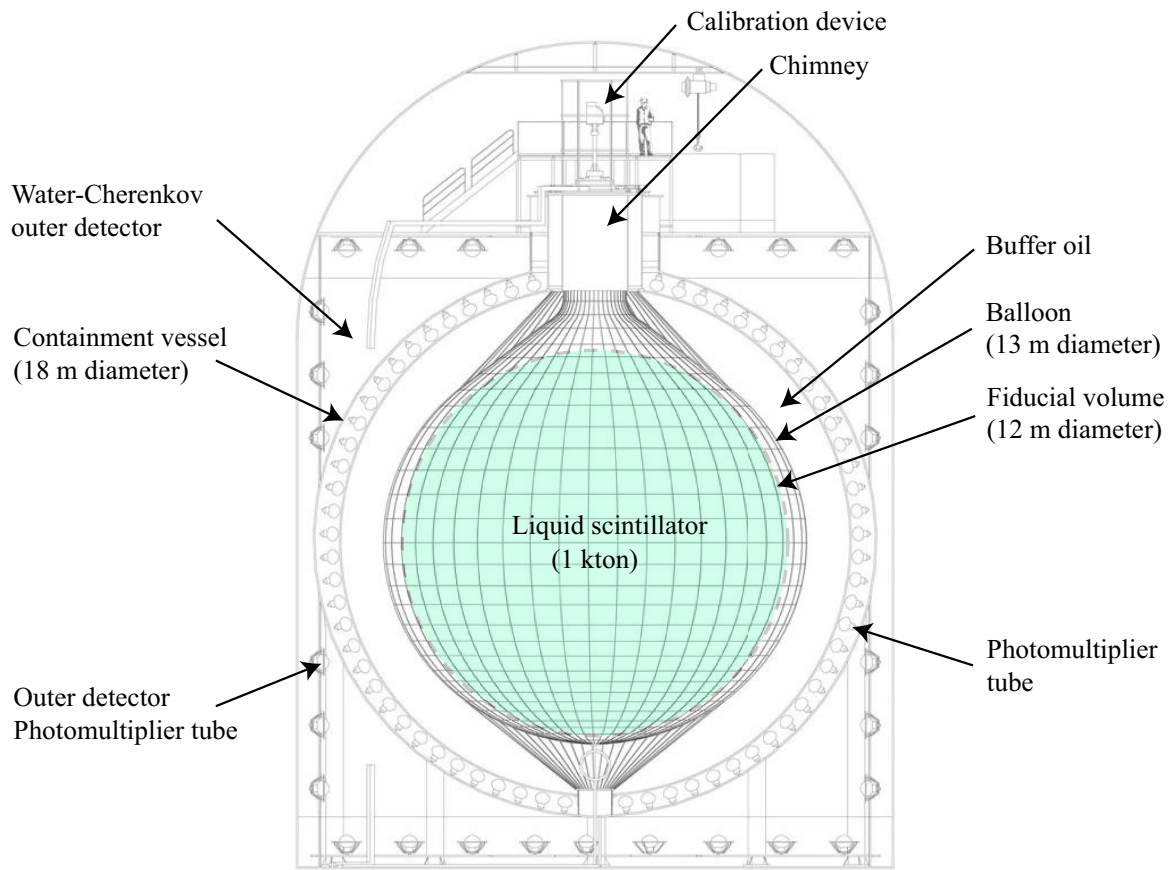Vogel, P., Schenter, G. K., Mann, F. M., & Schenter, R. E. 1981, Phys. Rev. C, 24, 1543

Calibration device

Chimney

Water-Cherenkov
outer detector

Buffer oil

Balloon
(13 m diameter)

Containment vessel
(18 m diameter)

Fiducial volume
(12 m diameter)

Liquid scintillator
(1 kton)

Photomultiplier
tube

Outer detector
Photomultiplier tube

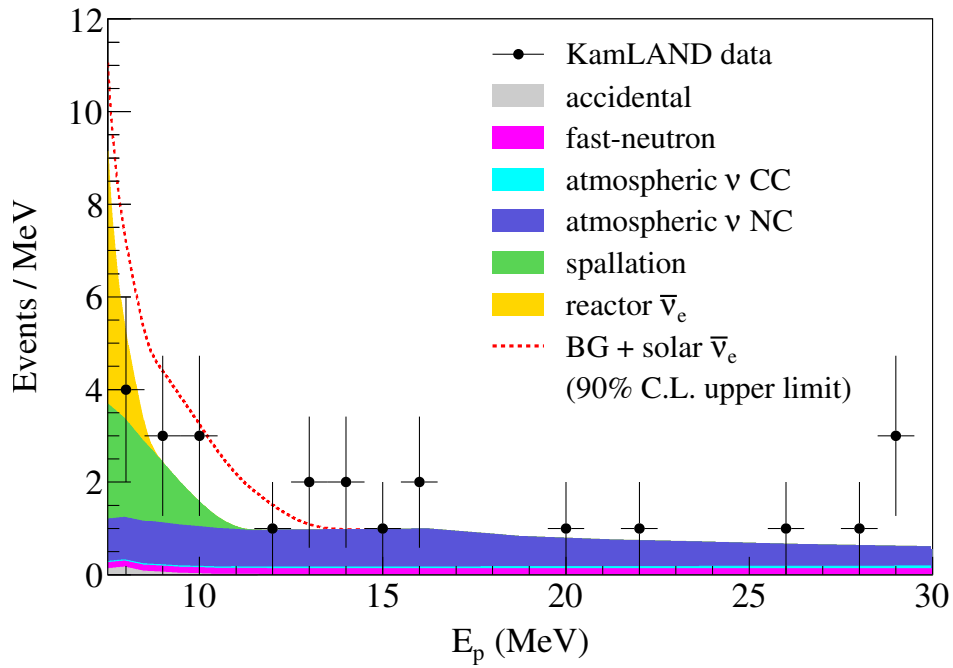Fig. 1.— Schematic diagram of the KamLAND detector.

Fig. 2.— Prompt energy distribution of selected $\overline{\nu}_e$ candidates together with the best-fit backgrounds (filled areas) and 90% C.L. upper limit of solar $\overline{\nu}_e$'s (red dashed line). The background histograms are cumulative.
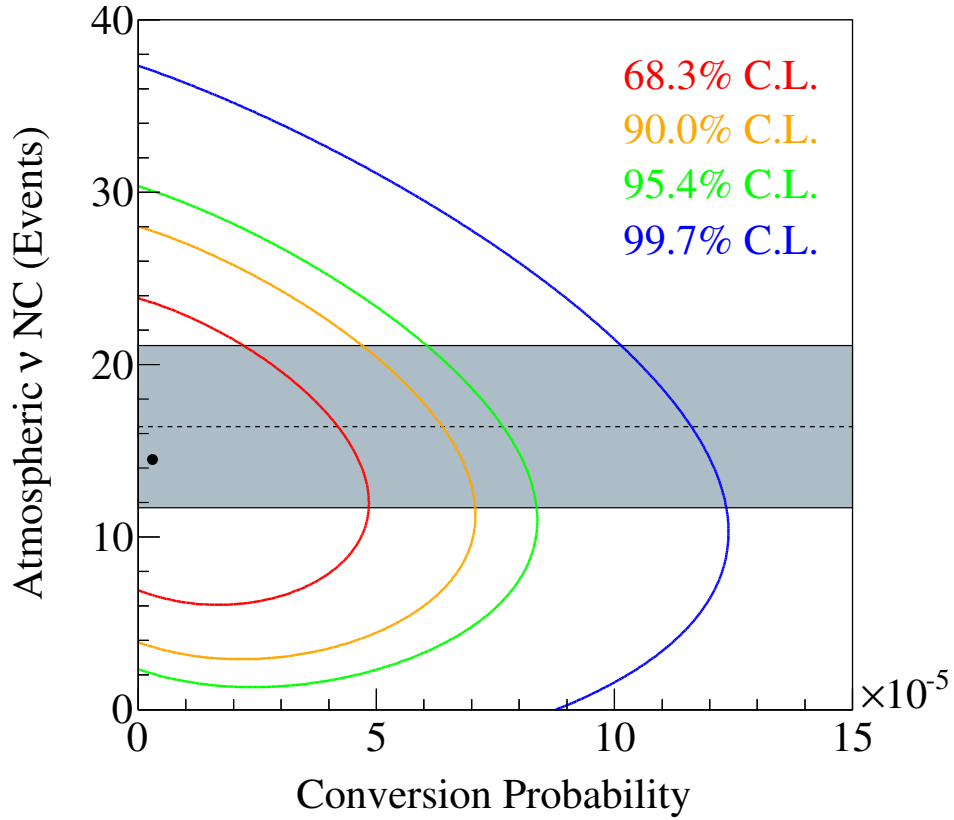
Fig. 3.— Allowed region, with the best-fit point, for the unconstrained neutral current (NC) background and the probability of solar neutrino conversion from the KamLAND data in the energy range of $8.3 \, \mathrm{MeV} < E_{\overline{\nu}_e} < 30.8 \, \mathrm{MeV}$. The confidence level (C.L.) is shown for two degrees of freedom. The gray shaded region indicates the $\pm 1\sigma$ prediction from the NC background calculation.
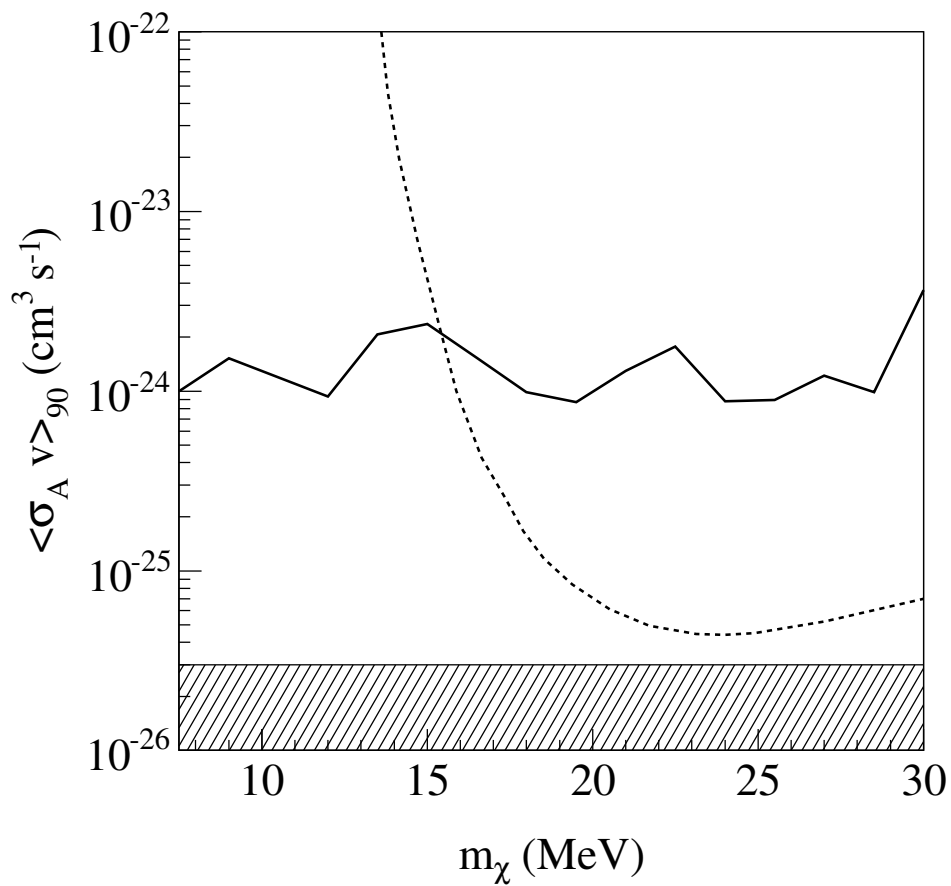
Fig. 4.— Upper limits at 90% C.L. on the dark matter annihilation cross section from KamLAND (solid line) and Super-Kamiokande (dashed line) (Palomares-Ruiz & Pascoli 2008). The shaded curve shows the natural scale of the annihilation cross section.
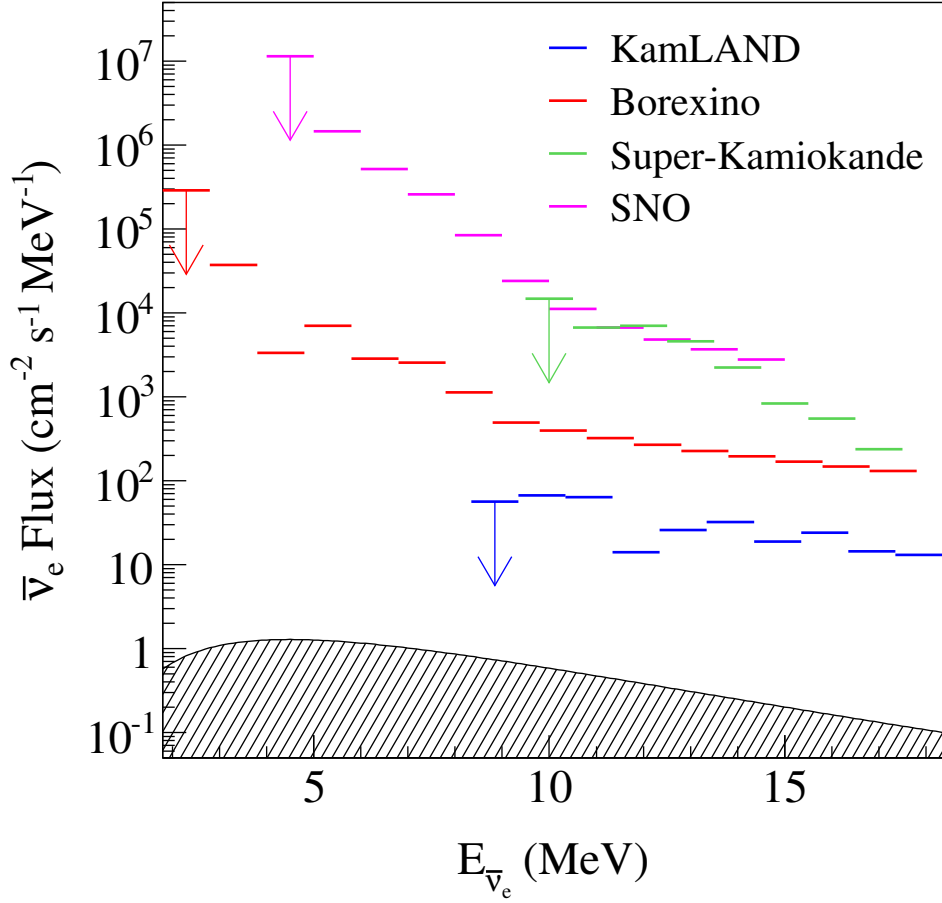
Fig. 5.— Model independent upper limits at 90% C.L. on the $\overline{\nu}_e$ flux from KamLAND (blue line), Borexino (Bellini et al. 2011) (red line), SNO (Aharmim et al. 2004) (magenta line), and Super-Kamiokande (Gando et al. 2003) (green line). The shaded curve shows the diffuse supernova $\overline{\nu}_e$ flux for the reference model prediction (Ando & Sato 2004).

Table 1.   Calculated backgrounds for atmospheric neutrino CC interactions with prompt energy between 7.5 MeV and 30.0 MeV.

Reaction	Number of events
$\nu_\mu + {}^{12}\mathrm{C} \to \mu^- + n + {}^{11}\mathrm{N}$	0.4
$\overline{\nu}_\mu + {}^{12}\mathrm{C} \to \mu^+ + n + {}^{11}\mathrm{B} + \gamma$	0.4
$\overline{\nu}_\mu + {}^{12}\mathrm{C} \to \mu^+ + n + {}^{7}\mathrm{Li} + \alpha$	0.4
$\overline{\nu}_\mu + {}^{12}\mathrm{C} \to \mu^+ + 2n + {}^{10}\mathrm{B}$	0.02
$\overline{\nu}_\mu + {}^{12}\mathrm{C} \to \mu^+ + n + {}^{11}\mathrm{B}$	0.7
$\overline{\nu}_\mu + p \to \mu^+ + n$	2.1
Total	4.0 ± 0.9

Table 2.   Summary of the estimated backgrounds with prompt energy between 7.5 MeV and 30.0 MeV.

Background	Number of events
Random coincidences	0.22 ± 0.01
Reactor $\overline{\nu}_e$	2.2 ± 0.7
${}^{9}\mathrm{Li}$	4.0 ± 0.3
Atmospheric ν (CC)	0.9 ± 0.2
Atmospheric ν (NC)	16.4 ± 4.7
Fast-neutron	3.2 ± 3.2
Total	26.9 ± 5.7

Table 3.   Model independent upper limit on the $\overline{\nu}_e$ flux for each energy bin from KamLAND, as shown in Fig. 5.

Energy Range (MeV)	Upper Limit at 90% C.L. ($\mathrm{cm^{-2}s^{-1}}$)
8.3-9.3	56.2
9.3-10.3	67.1
10.3-11.3	83.8
11.3-12.3	14.0
12.3-13.3	25.8
13.3-14.3	32.2
14.3-15.3	18.9
15.3-16.3	24.1
16.3-17.3	14.5
17.3-18.3	13.0